

# Comparison of the Uniformity and Efficiency of the Square and Circular Helmholtz Coils for Wireless Power Transmission System

Zenglei Zhang<sup>1</sup>, Changshun Yuan<sup>2</sup>, Jinyang Gao<sup>1, \*</sup>, Chen Gao<sup>1</sup>, and Jinshan Zhou<sup>1</sup>

**Abstract**—Wireless power transmission system (WPTS) based on near-field inductive coupling is an effective way to provide power for gastrointestinal micro-robot. WPTS is normally realized by a Helmholtz coil outside the body and a three-dimensional receiving coil in the micro-robot. Helmholtz coil has two types, circle and square. However, a quantitative comparison for them in the application of WPTS has not been available yet. In this paper, the calculating models of the electromagnetic field intensity (EMFI) for the circular Helmholtz coil (CHC) and square Helmholtz coil (SHC) are built. With the built model, the uniformities of the electromagnetic field (UEMF) of two Helmholtz coils are calculated. The actual coil system is built to verify the correctness of the built models. When the diameter of the CHC and the side length of the SHC are both 40 cm, the available areas (UEMF  $\geq 90\%$ ) for powering the robot supplied by the CHC and SHC are 39% and 56%, respectively. Also, the consumed powers of the two coils, when identical EMFI is excited, are compared. When the EMFI at the center of the CHC and SHC are both 1 Gs, the consumed powers are 5.09 W and 4.62 W, respectively. The above results show that compared to the CHC, the SHC not only has better uniformity, but also consumes less power. Thus, it is more suitable for the WPTS.

## 1. INTRODUCTION

Gastrointestinal micro-robot is currently a hotspot in the field of the endoscope medical equipment [1–4]. It can actively moves in gastrointestinal tract and performs comprehensive diagnosis [5]. It allows doctors to diagnose various diseases related to gastrointestinal tract, such as tumor, bleeding, and ulcer [6]. However, power supply is one of the bottlenecks for gastrointestinal micro-robot, because a power cable can cause a friction in the intestine, and a button battery has limited capacity which is not sufficient to power a gastrointestinal micro-robot for a long duration [7]. The wireless power transmission system (WPTS) based on near-field inductive coupling principle has been proven promising to solve this problem [8–10]. WPTS is realized by the Helmholtz coil outside the body and three-dimensional receiving coil in the micro-robot. The former excites alternating electromagnetic fields, and the latter induces an alternating electromagnetic field to generate an induced electromotive force [11, 12]. The power for a gastrointestinal micro-robot is provided by induced electromotive force through rectification and stabilization. At present, significant research efforts have been dedicated to develop an efficient WPTS [13–15]. However, the existing studies did not fully provide a clear analytical model for the electromagnetic field intensity (EMFI) of a square Helmholtz coil (SHC). And for circular Helmholtz coil (CHC) and SHC, a quantitative comparison concerning their uniformities of the electromagnetic field (UEMFs), as well as the consumed power when they excite identical electromagnetic field intensity (EMFI), has not been available yet.

---

*Received 22 March 2021, Accepted 9 April 2021, Scheduled 20 April 2021*

\* Corresponding author: Jinyang Gao (gjy.1001@163.com).

<sup>1</sup> Science and Technology on Electronic Test and Measurement Laboratory, North University of China, Taiyuan 030051, China.

<sup>2</sup> Hangzhou Innovation Institute, Beihang University, Hangzhou 310051, China.

To address the above mentioned problems, in this paper, based on Biot-Savart's Law and the theory of the wireless power transmission, the calculating models of the EMFI for the CHC and SHC are built. With the built models, the UEMFs of two Helmholtz coils are calculated. The correctness of the built models are verified by the actual coil system. Also, the UEMFs and consumed powers of the two Helmholtz coils are compared. Then, the SHC not only has better uniformity, but also consumes less power.

This paper is organized as follows. Section 2 presents the working principle of the WPTS. Section 3 describes the calculating models of the EMFI and UEMF for two Helmholtz coils. Experiment and results are given in Section 4. Conclusions are given in Section 5.

## 2. WORKING PRINCIPLE OF WPTS

When a gastrointestinal micro-robot is working, stable voltage needs to be provided by the receiving coil. The Helmholtz coil is required to provide a uniform electromagnetic field to the receiving coil. Therefore, the working principle of the WPTS and the relationship between the induced electromotive force and the EMFI are analyzed.

The equivalent circuit of the WPTS based on near-field inductive coupling is shown in Figure 1, which includes a transmitter and a receiver.

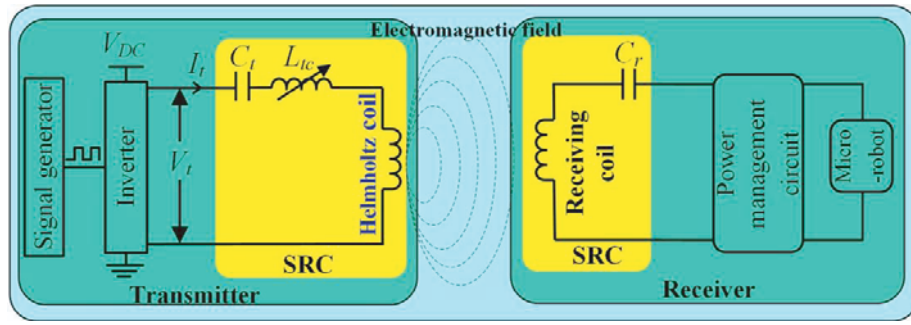


**Figure 1.** The equivalent circuit of the WPTS.

The transmitter includes three parts: series resonant circuit (SRC), signal generator, and inverter. SRC includes a Helmholtz coil, a resonant capacitor  $C_t$ , and an adjustable inductance  $L_{tc}$  that make the Helmholtz coil resonant. A signal generator is used to generate a square wave signal. An inverter converts DC voltage  $V_{DC}$  into AC voltage  $V_t$  under the control of the square wave signal. When AC pulse voltage  $V_t$  is loaded on SRC, due to the frequency-selection function of the SRC, a sinusoidal excitation current  $I_t (= I_m \sin(2\pi ft))$  where  $I_m$  is the peak driving current) will be generated in the Helmholtz coil. And the alternating electromagnetic field will be excited.

The receiver includes two parts, SRC and power management circuit. SRC includes a receiving coil and a resonant capacitor  $C_r$  that makes the receiving coil resonate. The induced electromotive force of the receiving coil is generated by inducing alternating electromagnetic field. The stable voltage (processed by the power management circuit) is provided to the gastrointestinal micro-robot.

In order to analyze the relationship between the induced electromotive force and EMFI, the largest plane (that is,  $XOY$  plane) parallel to the ground plane in the electromagnetic field of the Helmholtz coil is chosen. The simplified model of the Helmholtz coil and  $XOY$  plane are shown in Figure 2. According to Faraday's law of electromagnetic induction, the relationship between the induced electromotive force and the EMFI can be expressed as

$$\varepsilon(x, y, 0) = kn\omega S |B(x, y, 0)| \quad (1)$$

where  $\varepsilon(x, y, 0)$  is the induced electromotive force of the receiving coil at any point  $P$  on the  $XOY$  plane,  $B(x, y, 0)$  the EMFI at any point  $P$  on the  $XOY$  plane,  $n$  the number of turns for the receiving coil,  $S$  the cross-sectional area of the receiving coil,  $k$  the enhancement factor of the ferrite core in the receiving coil, and  $\omega (= 2\pi ft)$  the angular frequency of the excitation current  $I_t$ .

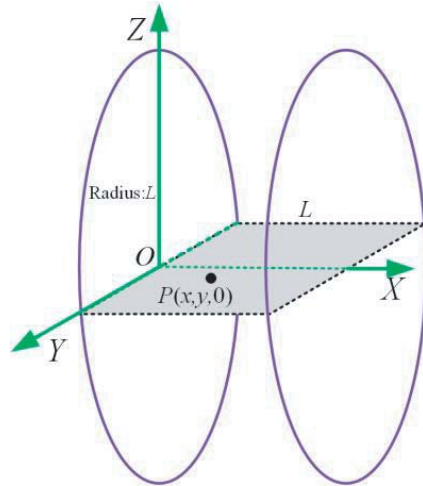


**Figure 2.** The simplified model of the Helmholtz coil and the  $XOY$  plane.

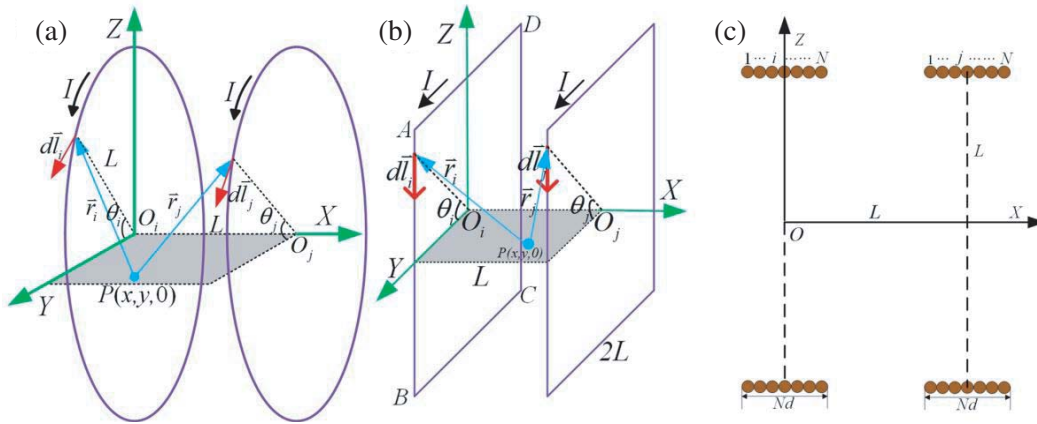


**Figure 3.** (a) The simplified coil model of the CHC, (b) the simplified coil model of the SHC, and (c) the complete coil model for the CHC and SHC.

### 3. MODEL OF THE EMFI FOR THE CHC AND SHC

Figure 3 shows the simplified and completed coil model for the CHC and SHC.

In Figure 3(a) and Figure 3(b),  $I$  is the amplitude of the current of the Helmholtz coil, and  $I = 1$  A. The angle between the infinitesimal current  $Id\vec{l}_i$  and the  $XOY$  plane is  $\theta_i$ . Similarly, the angle between the infinitesimal current  $Id\vec{l}_j$  and the  $XOY$  plane is  $\theta_j$ . The vector from any point  $P(x, y, 0)$  on the  $XOY$  plane to the infinitesimal current  $Id\vec{l}_i$  is  $\vec{r}_i$ . Similarly, the vector from any point  $P(x, y, 0)$  on the  $XOY$  plane to the infinitesimal current  $Id\vec{l}_j$  is  $\vec{r}_j$ . The radius of the CHC is  $L$ , and the side length of the SHC is  $2L$ . In Figure 3(b), on the SHC, each turn of the coil is divided into four segments: AD, DC, CB, and BA. In Figure 3(c), the center distance between the two sides of the coil is  $L$ ; the number of turns of the single-sided coil is  $N$ ,  $N = 24$ ; the diameter  $d$  of the litz wire is 1.8 mm.

According to Biot-Savart's Law, the EMFI  $B_P$  at point  $P$  on the  $XOY$  plane is equal to the vector sum of the EMFI of the coils on both sides at this point. The EMFI  $B_P$  at point  $P$  can be expressed as

$$\vec{B}_P = \frac{N\mu_0}{4\pi} \left( \int_{l_i} \frac{Id\vec{l}_i \times \vec{r}_i}{|r_i|^3} + \int_{l_j} \frac{Id\vec{l}_j \times \vec{r}_j}{|r_j|^3} \right) \quad (2)$$

where  $\mu_0$  is the vacuum permeability, and its value is  $4\pi \times 10^{-7}$ .

Also, the EMFI  $\vec{B}_P$  at any point  $P$  is equal to the vector sum of the EMFI at the  $X$ ,  $Y$ , and  $Z$  axes. That is,

$$\vec{B}_P = \vec{B}_x + \vec{B}_y + \vec{B}_z \quad (3)$$

According to right hand grip rule, the main component of the EMFI for the Helmholtz coil is at the  $X$ -axis direction. Therefore, in this paper, the EMFI at the  $X$ -axis direction is analyzed.

### 3.1. The EMFI of the Circular Helmholtz Coil

In Figure 3(a), on the  $i$ -th turn of the left part for the CHC, the coordinate of the infinitesimal current  $I\vec{d}\vec{l}_i$  at the angle  $\theta_i$  is  $((i - \frac{N+1}{2})d, L \cos \theta_i, L \sin \theta_i)$ ; infinitesimal current  $I\vec{d}\vec{l}_i$  is  $(0, -IL \sin \theta_i d\theta_i, IL \cos \theta_i d\theta_i)$ ; the vector  $\vec{r}_i$  from point  $P(x, y, 0)$  to the infinitesimal current  $I\vec{d}\vec{l}_i$  is  $((i - \frac{N+1}{2})d - x, L \cos \theta_i - y, L \sin \theta_i)$ . Therefore, on the left part of the CHC, the EMFI of the point  $P$  at the  $X$ -axis direction can be calculated as

$$B_{\text{circular-}x\text{-}i} = \frac{\mu_0 I}{4\pi} \sum_{i=1}^N \int_0^{2\pi} \frac{Ly \cos \theta_i - L^2}{|r_i|^3} d\theta_i \quad (4)$$

Similarly, on the  $j$ -th turn of the right part for the CHC, the coordinate of the infinitesimal current  $I\vec{d}\vec{l}_j$  at the angle  $\theta_j$  is  $((j - \frac{N+1}{2})d + L, L \cos \theta_j, L \sin \theta_j)$ ; infinitesimal current  $I\vec{d}\vec{l}_j$  is  $(0, -IL \sin \theta_j d\theta_j, IL \cos \theta_j d\theta_j)$ ; the vector  $\vec{r}_j$  from point  $P(x, y, 0)$  to the infinitesimal current  $I\vec{d}\vec{l}_j$  is  $((j - \frac{N+1}{2})d + L - x, L \cos \theta_j - y, L \sin \theta_j)$ . Therefore, on the right part of the CHC, the EMFI of the point  $P$  at the  $X$ -axis direction can be calculated as

$$B_{\text{circular-}x\text{-}j} = \frac{\mu_0 I}{4\pi} \sum_{j=1}^N \int_0^{2\pi} \frac{Ly \cos \theta_j - L^2}{|r_j|^3} d\theta_j \quad (5)$$

For the CHC, the EMFI of the point  $P$  at the  $X$ -axis direction can be expressed as

$$B_{\text{circular-}x} = B_{\text{circular-}x\text{-}i} + B_{\text{circular-}x\text{-}j} \quad (6)$$

### 3.2. The EMFI of the Square Helmholtz Coil

In Figure 3(b), on the  $i$ -th turn of the left part for the SHC, at AD, DC, CB, and BA segments, the coordinates of the infinitesimal current  $I\vec{d}\vec{l}_i$  at the angle  $\theta_i$  are  $((i - \frac{N+1}{2})d, L \cot \theta_i, L)$ ,  $((i - \frac{N+1}{2})d, -L, -L \tan \theta_i)$ ,  $((i - \frac{N+1}{2})d, -L \cot \theta_i, -L)$ , and  $((i - \frac{N+1}{2})d, L, L \tan \theta_i)$ ; the infinitesimal currents  $I\vec{d}\vec{l}_i$  are  $(0, -IL \csc^2 \theta_i d\theta_i, 0)$ ,  $(0, 0, -IL \sec^2 \theta_i d\theta_i)$ ,  $(0, IL \csc^2 \theta_i d\theta_i, 0)$ , and  $(0, 0, IL \sec^2 \theta_i d\theta_i)$ ; the vectors from point  $P(x, y, 0)$  to the infinitesimal current  $I\vec{d}\vec{l}_i$  are  $\vec{r}_{i-1}$ ,  $\vec{r}_{i-2}$ ,  $\vec{r}_{i-3}$ ,  $\vec{r}_{i-4}$ ; the values are  $((i - \frac{N+1}{2})d - x, L \cot \theta_i - y, L)$ ,  $((i - \frac{N+1}{2})d - x, -L - y, -L \tan \theta_i)$ ,  $((i - \frac{N+1}{2})d - x, -L \cot \theta_i - y, -L)$ , and  $((i - \frac{N+1}{2})d - x, L - y, L \tan \theta_i)$ . Therefore, on the left part of the SHC, the EMFI of the point  $P$  at the  $X$ -axis direction can be calculated as

$$B_{\text{square-}x\text{-}i} = \frac{\mu_0 I}{4\pi} \sum_{i=1}^N \left( \begin{aligned} & \int_{\pi/4}^{3\pi/4} \frac{-L^2 \csc^2 \theta_i}{|r_{i-1}|^3} d\theta_i + \int_{3\pi/4}^{5\pi/4} \frac{(-Ly \sec^2 \theta_i - L^2 \sec^2 \theta_i)}{|r_{i-2}|^3} d\theta_i \\ & + \int_{5\pi/4}^{7\pi/4} \frac{-L^2 \csc^2 \theta_i}{|r_{i-3}|^3} d\theta_i + \int_{7\pi/4}^{9\pi/4} \frac{(Ly \sec^2 \theta_i - L^2 \sec^2 \theta_i)}{|r_{i-4}|^3} d\theta_i \end{aligned} \right) \quad (7)$$

Similarly, on the  $j$ -th turn of the right part for the SHC, at AD, DC, CB, and BA segments, the coordinates of the infinitesimal current  $I\vec{d}\vec{l}_j$  at the angle  $\theta_j$  are  $((j - \frac{N+1}{2})d + L, L \cot \theta_j, L)$ ,  $((j - \frac{N+1}{2})d + L, -L, -L \tan \theta_j)$ ,  $((j - \frac{N+1}{2})d + L, -L \cot \theta_j, -L)$ , and  $((j - \frac{N+1}{2})d + L, L, L \tan \theta_j)$ ; the

infinitesimal currents  $Id\vec{l}_j$  are  $(0, -IL \csc^2 \theta_j d\theta_j, 0)$ ,  $(0, 0, -IL \sec^2 \theta_j d\theta_j)$ ,  $(0, IL \csc^2 \theta_j d\theta_j, 0)$ , and  $(0, 0, IL \sec^2 \theta_j d\theta_j)$ ; the vectors from point  $P(x, y, 0)$  to the infinitesimal current  $Id\vec{l}_j$  are  $\vec{r}_{j-1}$ ,  $\vec{r}_{j-2}$ ,  $\vec{r}_{j-3}$ ,  $\vec{r}_{j-4}$ ; the values are  $((j - \frac{n+1}{2})d + L - x, L \cot \theta_j - y, L)$ ,  $((j - \frac{n+1}{2})d + L - x, -L - y, -L \tan \theta_j)$ ,  $((j - \frac{n+1}{2})d + L - x, -L \cot \theta_j - y, -L)$ ,  $((j - \frac{n+1}{2})d + L - x, L - y, L \tan \theta_j)$ . Therefore, on the right part of the SHC, the EMFI of the point  $P$  at the  $X$ -axis direction can be calculated as

$$B_{\text{square-}x-j} = \frac{\mu_0 I}{4\pi} \sum_{j=1}^N \left( \int_{\pi/4}^{3\pi/4} \frac{-L^2 \csc^2 \theta_j}{|r_{j-1}|^3} d\theta_j + \int_{3\pi/4}^{5\pi/4} \frac{(-Ly \sec^2 \theta_j - L^2 \sec^2 \theta_j)}{|r_{j-2}|^3} d\theta_j \right. \\ \left. + \int_{5\pi/4}^{7\pi/4} \frac{-L^2 \csc^2 \theta_j}{|r_{j-3}|^3} d\theta_j + \int_{7\pi/4}^{9\pi/4} \frac{(Ly \sec^2 \theta_j - L^2 \sec^2 \theta_j)}{|r_{j-4}|^3} d\theta_j \right) \quad (8)$$

For the SHC, the EMFI of the point  $P$  at the  $X$ -axis direction can be expressed as

$$B_{\text{square-}x} = B_{\text{square-}x-i} + B_{\text{square-}x-j} \quad (9)$$

### 3.3. The Uniformity of the Electromagnetic Field

The variation tendency of the EMFI between point  $P$  and the center on  $XOY$  plane is reflected by the UEMF. The UEMF at point  $P$  can be expressed as

$$UEMF = \left( 1 - \left| \frac{(B_P - B_{\text{center}})}{B_{\text{center}}} \right| \right) \times 100\% \quad (10)$$

where  $B_{\text{center}}$  is the EMFI at the center on the  $XOY$  plane.

The UEMF is reflected by the proportion of the available area. When the UEMF  $\geq 90\%$ , the largest rectangle on the  $XOY$  plane that can be obtained is the available area, and when the receiving coil works in the available area, the transmitting efficiency can basically remain stable. The proportion of the available area can be expressed as

$$\eta = \frac{S_{\text{available-area}}}{S_{\text{total-area}}} \times 100\% \quad (11)$$

For the CHC, the total area is equal to the diameter multiplied by the center distance between the two sides of the coil, and for the SHC, the total area is equal to the side length multiplied by the center distance between the two sides of the coil.

## 4. EXPERIMENTS AND RESULTS

### 4.1. Experimental Setup

To verify the analysis above, the experimental setup shown in Figure 4 is designed, which includes an one-dimensional circular Helmholtz coil, an one-dimensional square Helmholtz coil, a three-dimensional detection coil, a circuit that drives the Helmholtz coil, a full space adjusting device, and an oscilloscope.

For the Helmholtz coils, the diameter of the CHC and the side length of the SHC are both 40 cm. The center distances between the two sides of coil are both 20 cm. The number of turns for the single-sided coil is 24. The electrical parameters of two Helmholtz coils measured by the LCR instrument are listed in Table 1. Two Helmholtz coils are wound with Litz wire (180 strands of AWG38 enameled copper wire).

**Table 1.** The electrical parameters measured by the LCR.

The electrical parameters	The CHC	The SHC
Quality factor $Q$	893	803
AC resistance $R_s(\Omega)$	1.41	1.89
Inductance $L_s$ (mH)	0.911	1.085

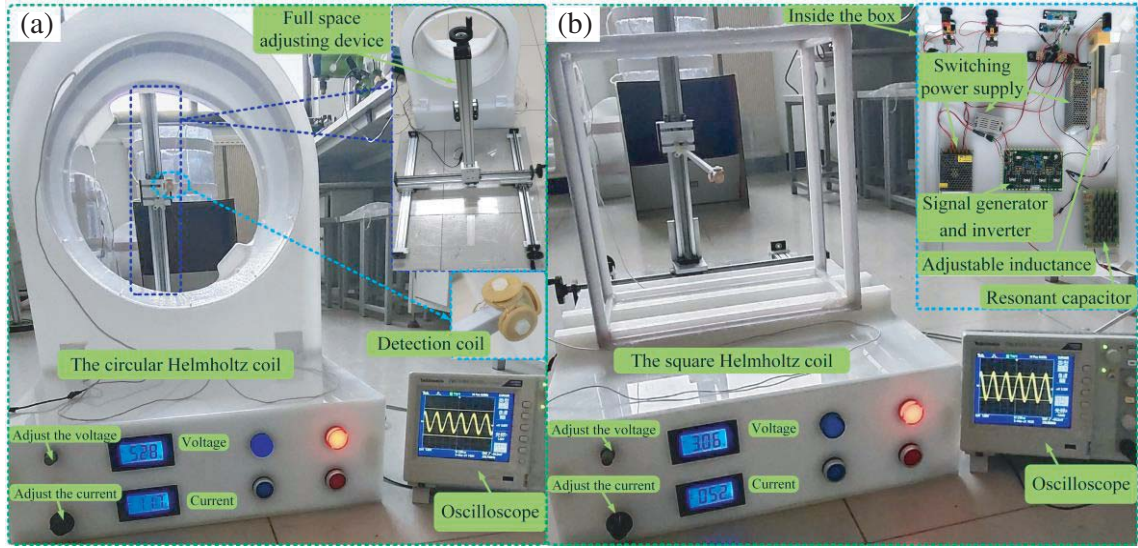


**Figure 4.** Experimental setup, (a) the CHC and (b) the SHC.

The three-dimensional detection coil includes three orthogonal circular coils. The diameters of the circular coil are both 14 mm, and the numbers of turns are both 48. Detection coil is wound with enameled wire (wire diameter = 0.15 mm).

The driving circuit includes a signal generator, an inverter, a resonant capacitor, an adjustable inductor, a switching power supply, a voltmeter, and an ammeter. Through the full space adjusting device, the three-dimensional detection coil can detect the EMFI at any position on the  $XOY$  plane.

## 4.2. Results and Discussion

Using the experimental setup shown in Figure 4, two experiments are carried out: one for verifying the calculating model of the EMFI and comparing the UEMFs of two Helmholtz coils, and the other for comparing the consumed powers of two Helmholtz coils. In the experiments: The  $XOY$  plane of the Helmholtz coil is divided into 800 regions, each with an area of  $1 \text{ cm}^2$ , and the induced voltage of the detection coil in each region is measured; the transmission frequency  $f$  of this transmitting coil was selected as 218 kHz with consideration of improving power transmitting efficiency [16].

### 4.2.1. The Results of the EMFI

With Equations (4) to (9) and the calculating software MATLAB R2020a, the EMFI distributions of the CHC and SHC are calculated, as shown in Figure 5. The measured results are also plotted in Figure 5 for comparison. To make the comparison clear, Table 2 lists the maximum and minimum values of the EMFI, as well as the EMFI at the center of the coil. It can be found that the measured values is consistent with the calculated ones, thus manifesting the correctness of the built model.

**Table 2.** The calculated and measured values of the EMFI.

The EMFI (Gs)	The CHC		The SHC	
	Calculated	Measured	Calculated	Measured
Center	1.0133	1.0227	1.0133	1.0114
Max	3.5083	3.0143	3.2849	2.7863
Min	0.4491	0.4991	0.4623	0.5064

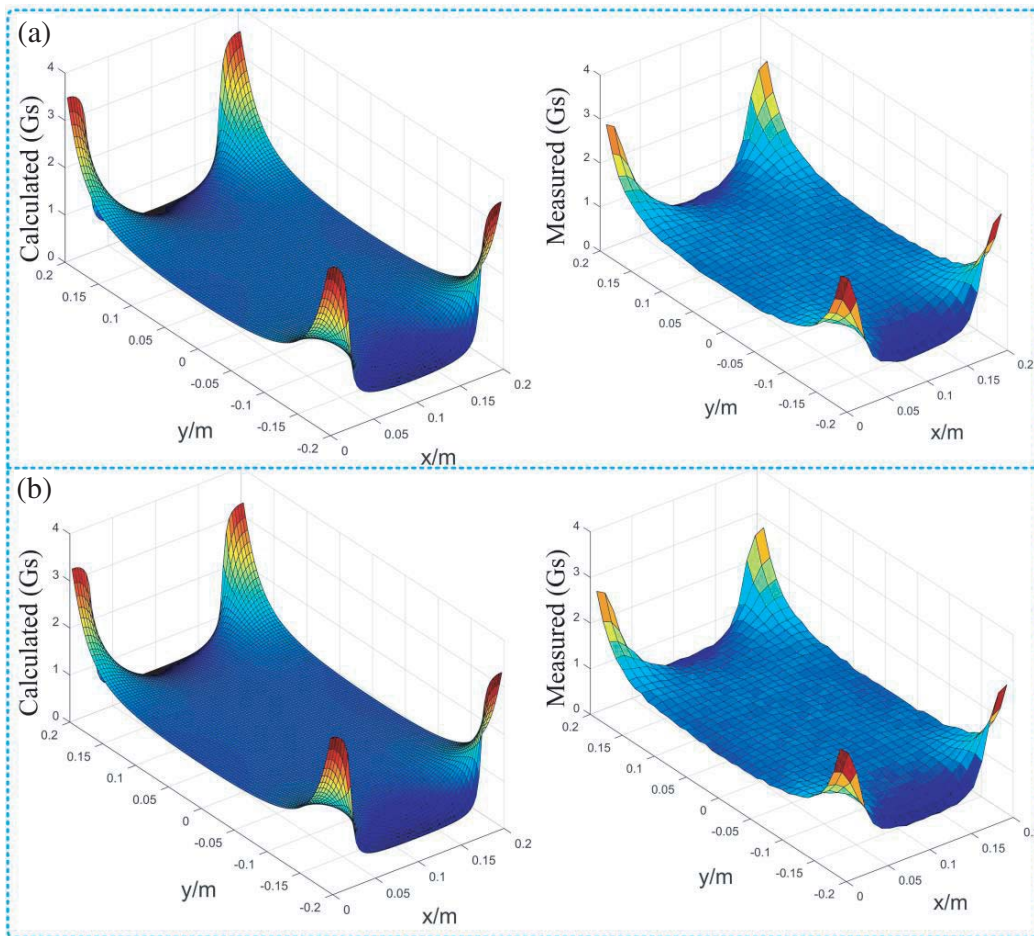


**Figure 5.** Calculated and measured values of the EMFI, (a) the CHC and (b) the SHC.

4.2.2. The Results of the UEMF

When the diameter of the CHC and the side length of the SHC are both 40 cm, and the UEMFs are both  $\geq 90\%$ , the available areas for the CHC and SHC are compared. The calculated and measured values of the UEMF are shown in Figure 6. The available area is reflected by the red rectangle. The calculated and measured values of the available area are listed in Table 3. The experimental result shows that the measured value is consistent with the calculated value. Thus, the correctness of the UEMF is verified by experiment, and the electromagnetic field of the SHC has better uniformity.

**Table 3.** The calculated and measured values for the available area.

The available area	The CHC		The SHC	
	Calculated	Measured	Calculated	Measured
	40%	39%	58.33%	56%

4.2.3. The Results of the Consumed Power

For the experiment of the consumed power, the three-dimensional detection coil is placed at the center on the  $XOY$  plane. Then the EMFIs of the Helmholtz coil are adjusted by an adjustable inductor  $L_{tc}$ .

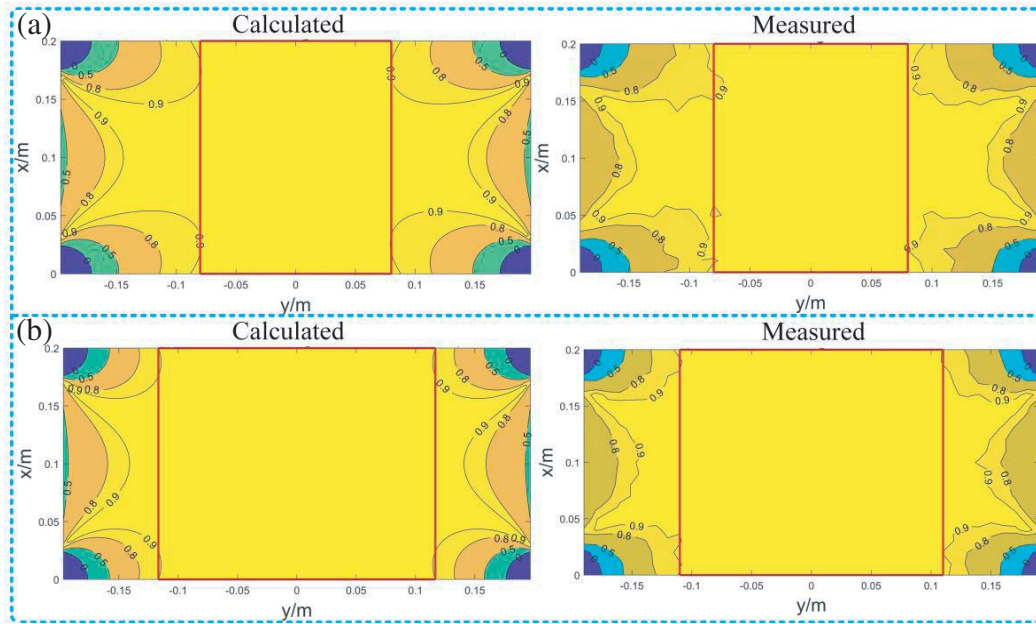


**Figure 6.** Calculated and measured values of the UEMF, (a) the CHC, (b) the SHC.

When the EMFIs at the centers of the CHC and SHC are both 1 Gs, and the consumed powers are 5.09 W and 4.62 W. Thus, compared to the CHC, the SHC consumes less power. The main reason is that the inductance of the SHC is greater than the CHC when the diameter of the CHC and the side length of the SHC are both 40 cm (shown in Table 1).

In summary, compared to the CHC, the SHC not only has better uniformity, but also consumes less power.

## 5. CONCLUSION

In this paper, based on Biot-Savart's Law and the theory of the WPTS, the calculating models of the EMFI for the CHC and SHC were built, and the UEMFs of two Helmholtz coils were calculated. The built models were validated by experiment. Also, the consumed powers of the two coils were compared. The experimental results indicate that when the diameter of the CHC and the side length of the SHC are both 40 cm, the available area for powering the robot supplied by the CHC and SHC are 39% and 56%; in addition, the consumed powers are 5.09 W and 4.62 W when the EMFIs at the center of the CHC and SHC are both 1 Gs. Thus, compared to the CHC, the SHC not only has better uniformity, but also consumes less power.

## ACKNOWLEDGMENT

This work was supported by the National Natural Science Foundation of China (Grant No. 61803347), by Shanxi Province Science Foundation for Youths (Grant No. 201801D221201), by Youth Academic Leader Support Project of North University of China (Grant No. QX201808), by Key Research and Development Plan of Shanxi Province under Contract 201903D321164, by Scientific and Technological Innovation Programs of Higher Education Institutions in Shanxi under Contract 2019L0512, and by the Opening Foundation of Shanxi Key Laboratory of Advanced Manufacturing Technology under Contract XJZZ201803.

## REFERENCES

1. Gao, J., G. Yan, Y. Shi, H. Cao, K. Huang, H. Gao, and J. Liu, "Analysis of connection way of a three-dimensional receiving coil onboard a capsule robot for wireless power transmission," *Progress In Electromagnetics Research M*, Vol. 78, 39–48, 2019.
2. Guo, S., Q. Yang, L. Bai, and Y. Zhao, "Development of multiple capsule robots in pipe," *Micromachines*, Vol. 9, No. 6, 259–274, 2018.
3. Gao, J., G. Yan, S. He, F. Xu, and Z. Wang, "Design, analysis, and testing of a motor-driven capsule robot based on a sliding clasper," *Robotica*, Vol. 35, 521–536, 2017.
4. Park, H., D. Kim, and B. Kim, "A robotic colonoscope with long stroke and reliable leg clamping," *International Journal of Precision Engineering and Manufacturing*, Vol. 13, No. 8, 1461–1466, 2012.
5. Basar, M. R., F. Malek, K. M. Juni, M. S. Idris, and M. Saleh, "Ingestible wireless capsule technology: A review of development and future indication," *International Journal of Antennas and Propagation*, Vol. 2012, No. 4, 1548–1551, 2012.
6. Moglia, A., A. Menciassi, P. Dario, and A. Cuschieri, "Capsule endoscopy: Progress update and challenges ahead," *Nature Reviews Gastroenterology & Hepatology*, Vol. 6, No. 6, 353–362, 2009.
7. Ciuti, G., A. Menciassi, and P. Dario, "Capsule endoscopy: from current achievements to open challenges," *IEEE Reviews in Biomedical Engineering*, Vol. 4, 59–72, 2012.
8. Baser, M. R., M. Y. Ahmad, J. Cho, and F. Ibrahim, "An improved resonant wireless power transfer system with optimum coil configuration for capsule endoscopy," *Sensors and Actuators A: Physical*, Vol. 249, 207–216, 2016.
9. Basar, M. R., M. Y. Ahmad, J. Cho, and F. Ibrahim, "Stable and high-efficiency wireless power transfer system for robotic capsule using a modified Helmholtz coil," *IEEE Transactions on Industrial Electronics*, Vol. 64, No. 2, 1113–1122, 2017.
10. Basar, M. R., M. Y. Ahmad, J. Cho, and F. Ibrahim, "An improved wearable resonant wireless power transfer system for biomedical capsule endoscope," *IEEE Transactions on Industrial Electronics*, Vol. 65, No. 10, 7772–7781, 2018.
11. Carta, R., G. Tortora, J. Thoné, B. Lenaerts, P. Valdastrì, A. Menciassi, P. Dario, and R. Puers, "Wireless powering for a self-propelled and steerable endoscopic capsule for stomach inspection," *Biosensors and Bioelectronics*, Vol. 25, No. 5, 845–851, 2010.
12. Jia, Z., G. Yan, Z. Wang, and H. Liu, "Efficiency optimization of wireless power transmission systems for active capsule endoscopes," *Physiological Measurement*, Vol. 32, No. 10, 1561–1573, 2011.
13. Gao, J. and G. Yan, "A novel power management circuit using a super-capacitor array for wireless powered capsule robot," *IEEE/ASME Transactions on Mechatronics*, Vol. 22, No. 3, 1444–1455, 2017.
14. Luo, W., Q. Ke, G. Yan, and K. Yang, "Analytical computation of AC resistance of single-layer air-core Helmholtz coils," *Progress In Electromagnetics Research C*, Vol. 51, 111–119, 2014.
15. Gao, J., G. Yan, Z. Wang, S. He, F. Xu, P. Jiang, and D. Liu, "Design and testing of a motor-based capsule robot powered by wireless power transmission," *IEEE/ASME Transactions on Mechatronics*, Vol. 21, No. 2, 683–693, 2016.
16. Gao, J., G. Yan, Z. Wang, P. Jiang, and D. Liu, "A capsule robot powered by wireless power transmission: Design of its receiving coil," *Sensor. Actuat. A-Phys.*, Vol. 234, 133–142, Oct. 2015.